Hindawi
Journal of Chemistry
Volume 2023, Article ID 6683470, 13 pages
https://doi.org/10.1155/2023/6683470

Research Article

Natural Anthraquinones as Promising MAPK3 Inhibitors for Complementary Cancer Therapy

Samaneh Vaziri-Amjad,[1] **Massoud Moradi-Najmi**,[1] **and Amir Taherkhani**[2]

[1]*Department of Oral and Maxillofacial Medicine, School of Dentistry, Hamadan University of Medical Sciences, Hamadan, Iran*
[2]*Research Center for Molecular Medicine, Hamadan University of Medical Sciences, Hamadan, Iran*

Correspondence should be addressed to Amir Taherkhani; amir.007.taherkhani@gmail.com

Received 6 June 2023; Revised 14 July 2023; Accepted 26 July 2023; Published 7 August 2023

Academic Editor: Mohd Sajid Ali

Objective. MAPK3 activates several nuclear transcription factors, including c-Jun and c-fos, by phosphorylating its downstream cytoplasmic protein, thereby contributing to cell proliferation and survival. Different carcinomas' initiation, progression, cancer cell metastasis, and drug resistance have been associated with MAPK3 overexpression. Given the need for new and potent MAPK3 inhibitors, this study aimed to explore the potential of anthraquinones (AQs) as organic compounds capable of inhibiting MAPK3. *Methods*. Using AutoDock 4.0 software, the binding affinity of 21 AQs to the receptor's active site was evaluated. AQs were ranked based on their $\Delta G_{binding}$ values to the receptor's active site, with the highest rankings receiving the most favorable scores. The Discovery Studio Visualizer tool was used to demonstrate the interaction modes between the highest-ranked AQs and the MAPK3 catalytic site. Furthermore, a 100-nanosecond molecular dynamics (MD) computer simulation was performed to assess the stability of the docked pose of the most potent enzyme inhibitor identified in this study. *Results*. The binding affinity of emodin-8-glucoside, aloe-emodin 8-glucoside, pulmatin, rhodoptilometrin, and hypericin to the receptor's ATP binding cleft was noteworthy, as the $\Delta G_{binding}$ values were < -10 kcal/mol. In addition, emodin-8-glucoside, aloe-emodin 8-glucoside, and pulmatin were found to have inhibition constant values at the picomolar concentration. According to our computer simulation results, the docked pose of emodin-8-glucoside within the active site of MAPK3 achieved a stable state after 70 ns. In other words, the root mean square deviation (RMSD) graph indicated stability within the 70–100 ns timeframe. *Conclusion*. Inhibition of MAPK3 by emodin-8-glucoside, aloe-emodin 8-glucoside, pulmatin, rhodoptilometrin, and hypericin may have therapeutic potential in cancer treatment.

1. Introduction

Mitogen-activated protein kinases (MAPKs), a family of serine/threonine protein kinases, are highly conserved and have been shown to regulate a variety of cellular processes, including cellular differentiation, proliferation, survival, and apoptosis [1, 2]. It consists of multiple crucial components and phosphorylation events that significantly contribute to tumorigenesis. The activated kinases transmit signals from the extracellular environment, leading to cell growth, proliferation, differentiation, migration, and apoptosis [3]. As a critical signaling hub, the MAPK pathway integrates extracellular signals to regulate cellular differentiation, proliferation, and survival, as well as drug resistance [4, 5]. The pathway is composed of a range of kinases, including MAPKs (MAPK1 (ERK2) and MAPK3 (ERK1)), MEKs, RASs, RAFs, adaptor molecules, and specific negative regulators of ERK1/2 (DUSP3/5/6/7/9). The activation of MAPK1/3, KRAS, HRAS, and BRAF is widely recognized to contribute to several human cancers through transcriptional activation, interactions with other cancer-related pathways (e.g., JAK/STAT and PI3K pathways), and activities that modulate the immune response in some cancers [6–10]. Around 20% of cases of head and neck squamous cell carcinoma (HNSCC) exhibit activating mutations in the MAPK pathway [11]. Bayat et al. [12] reported that the MAPK1/MAPK3 signaling pathway has a noteworthy involvement in oral squamous cell carcinoma patients who

have a poor prognosis, as opposed to those with a favorable prognosis. The interaction between MAPK1 and MAPK3 with a complex network of structures is well established, and their role in promoting the malignant behavior of cancer cells by changing the metabolic signaling pathway is significant [13]. Several reports have defined MAPK3 as an oncogene factor in several malignancies, including breast, ovarian, colorectal, liver, lung, thyroid, and gastric cancers [14–18].

The ATP binding site of MAPK3, the kinase active site, is the target of type-I inhibitors. In contrast, type-II inhibitors bind to the allosteric pocket of enzymes, and these two groups make up the primary categories of kinase inhibitors [19].

Anthraquinones (compounds with a 9, 10-anthracene skeleton) are natural substances commonly employed in traditional Chinese medicine [20]. The biological properties of these compounds are multifaceted, encompassing antitumor, analgesic, antibacterial, antimalarial, antioxidant, and anti-inflammatory activities [21–23]. The outstanding antitumor activity demonstrated by anthraquinone derivatives has generated considerable interest recently, with inevitable results being authorized for clinical use as antitumor medications. Clinical compounds, including mitoxantrone, doxorubicin, daunorubicin, epirubicin, and emodin, are employed to treat a diverse range of cancers [24–27]. In this regard, the antitumor effect of mitoxantrone and doxorubicin has been attributed to their ability to induce apoptosis [28, 29]. The extraction of anthraquinones from *Damnacanthus* and *Morinda* spp. represents a promising avenue for obtaining natural anticancer compounds [30].

The present study proposes that AQs serve as effective inhibitors of MAPK3 activity. This inhibition can downregulate downstream signaling pathways, ultimately reducing cell differentiation and survival rate. Hence, a molecular docking analysis was conducted to assess the binding affinity of multiple AQs to the active site of MAPK3. The identification and introduction of the top-ranked MAPK3 inhibitors were based on the $\Delta G_{binding}$ values calculated between the AQs and the enzyme's active site. The subsequent step involved analyzing the interactions between the top-ranked AQs and residues present inside the MAPK3 catalytic cleft. Subsequently, the stability of the docked pose of the most effective MAPK3 inhibitor was compared with that of a standard drug using molecular dynamics (MD) simulation. The present outcomes hold promise for the development of cancer treatments.

2. Materials and Methods

2.1. Preparation of the Receptor and Ligands for Structural Analysis. Obtaining the 3D coordinates of MAPK3 (PDB ID, 4QTB; X-ray resolution, 1.4 Å) involved downloading from the RCSB database (https://www.rcsb.org, [31, 32]) and visualizing using BIOVIA Discovery Studio Visualizer (DSV) version 19.1.0.18287. Two polypeptide chains (A and B) with the same residues (348; 27–374) were present in the PDB file. Chain A was picked for in silico analyses, and the Notepad++ software was used to remove the water molecules and 38Z from the PDB file. The active site-interacting residues in 4QTB were determined by [1] examining the docked pose of 38Z using DSV software in a two-dimensional view and [2] referencing the publication by Chaikuad et al. [33]. The 4QTB file was subjected to energy minimization to attain its most stable 3D conformation using Swiss-PdbViewer version 4.1.0, which can be accessed at https://spdbv.unil.ch. By employing the GROMOS 43B1 force field, Swiss-pdbViewer can analyze the structure's energy and correct any irregular geometry via energy minimization. The selection of 21 AQs was made to explore potential MAPK3 inhibitors. An analysis of the MAPK3 ATP-binding cleft involved comparing the binding affinities of the studied AQs with that of ulixertinib (DB13930), a standard drug obtained from the DrugBank database (https://go.drugbank.com/, [34]). As part of our previous investigation [35], we followed an energy minimization procedure on the AQs. By adjusting the MAPK3 3D structure to include Kollman charges and polar hydrogen bonds and applying local charge and rotational motion to ligands structures, PDBQT files were generated for both the receptor and ligands using MGL tools [36].

2.2. Procedure for Docking Analysis. The setup used to conduct the docking analyses was a Windows-based PC with the subsequent specifications: 64-bit system type, 32 GB of installed RAM, and an Intel Core i7 processor [37]. Implementing the AutoDock version 4.0 tool and a semiflexible docking algorithm [38], the $\Delta G_{binding}$ values between AQs, a standard drug, and MAPK3 ATP-binding cleft were computed in kcal/mol units. Our earlier report [19] highlighted the presence of 29 residues in the ATP-binding cleft of MAPK3. As a result, the grid box was set up with the subsequent values for docking analysis: X-dimension, 84; Y-dimension, 60; Z-dimension, 70; X-center, 33.335 Å; Y-center, 55.015 Å; Z-center, 49.3 Å, and spacing, 0.375 Å. To assess the binding affinity between the studied AQs, the positive control inhibitor, and the MAPK3 active site, we constructed several independent docked models for each ligand using the Lamarckian genetic algorithm (GA) approach. The Lamarckian GA docking calculations utilized the following parameters: 50 GA runs, a population size of 150, a maximum number of evaluations set at 2500000, a maximum of 27000 generations, and only the top 1 individual automatically survives. The gene mutation rate was set at 0.02, while the crossover rate was set at 0.8, with a two-point crossover mode. The mean of the Cauchy distribution for gene mutation was set at 0.0, and the variance was set at 1.0. In addition, the worst individual was picked after 10 generations. The docking results were then grouped based on the root mean square (RMS) tolerance of 2.0 Å [36], and the most negative $\Delta G_{binding}$ value within the most significant cluster was chosen for evaluation. Finally, the generation of molecular visualizations was carried out using the DSV software.

2.3. Molecular Dynamics Analysis. The receptor was subjected to MD investigations alone and in complex with [1] the most highly ranked AQ from the molecular docking

results and [2] the standard drug ulixertinib. Computer simulations lasting 100 nanoseconds (ns) were employed to conduct MD analyses using Discovery Studio Client software version 16.1.0.15350. A more powerful computer configuration was employed for MD simulations than for docking analyses (system type, 64-bit; installed RAM, 64 GB DDR5; and processor, Intel 24-Core i9-13900KF). The MD simulation was conducted for 100 nanoseconds (100 ns) and implemented using advanced settings. The solvation model utilized was the explicit periodic boundary, while the cell shape was orthorhombic with a minimum distance set at 10 Å from the boundary. The solvent used was water, with a target temperature of 310 K. The force field utilized CHARMm, and the charge distribution was point-based [39, 40]. The root mean square deviation (RMSD) and root mean square fluctuation (RMSF) of the MAPK3 backbone atoms were investigated throughout MD simulations. In addition, the radius of gyration (ROG) and total energy of the receptor were computed to obtain more accurate outcomes.

3. Results

3.1. Binding Affinity Assessment. The top-ranking MAPK3 inhibitors were identified in this study by determining the $\Delta G_{binding}$ value of five AQs with the ATP-binding cleft, which was below −10 kcal/mol. The binding energies for emodin-8-glucoside, aloe-emodin 8-glucoside, pulmatin (chrysophanol-8-0-glucoside), rhodoptilometrin, and hypericin were calculated to be −12.78, −12.42, −12.41, −10.75, and −10.13 kcal/mol, respectively, highlighting their potential as effective inhibitors of MAPK3. The highly potent inhibitory effect of emodin-8-glucoside, aloe-emodin 8-glucoside, and pulmatin on MAPK3 was evident from the estimated *K*i value, within the picomolar (pM) range. On the other hand, rhodoptilometrin and hypericin exhibited inhibition at the nanomolar (nM) level, indicating their relatively weaker inhibitory potential. Based on the AutoDock 4.0 tool's calculation of the $\Delta G_{binding}$ value between ulixertinib and MAPK3, a total of 10 AQs, including top-ranked compounds as well as emodic acid, aloe-emodin, sennidin B, purpurin, and chrysophanol, exhibited a superior binding affinity to the MAPK3 catalytic site than the reference drug. The $\Delta G_{binding}$ value between ulixertinib and MAPK3 was found to be −9.12 kcal/mol (Figure 1). To provide a comprehensive overview of the ligand-MAPK3 affinity, Table 1 displays the calculated $\Delta G_{binding}$ and *K*i values between MAPK3 and all ligands. Furthermore, Table 2 presents a detailed analysis of all energy types computed between the ATP-binding site of MAPK3 and the top-ranked AQs. The Gibbs free energy of binding between a ligand and receptor is influenced by several energy factors, including intermolecular energy, internal energy, torsional free energy, and the unbound system's energy, which have been defined in previous reports [41, 42].

3.2. Evaluating Modes of Interaction. Through the DSV tool, the interactions between the top-ranked AQs, a reference drug, and residues positioned within the MAPK3 ATP cleft were revealed. Computer simulations lasting 100 ns were also conducted to explore the interactions between emodin-8-glucoside, ulixertinib, and residues located within the protein's active site. Among the ligands studied, emodin-8-glucoside, aloe-emodin 8-glucoside, and rhodoptilometrin formed the highest number of hydrogen bonds ($n = 5$), whereas rhodoptilometrin displayed the most hydrophobic interactions ($n = 6$) with the residues of MAPK3. The reference drug formed four hydrogen bonds and one hydrophobic interaction. Before the MD simulation, emodin-8-glucoside, the most effective MAPK3 inhibitor in this research, interacted with the residues of the MAPK3 ATP-binding cleft through five hydrogen bonds and five hydrophobic interactions. Nevertheless, this compound formed seven hydrogen bonds and three hydrophobic interactions after the MD simulation. The interactions between the ligands and the residues of the MAPK3 ATP-binding cleft are presented in Figure 2 and summarized in Table 3. Notably, Table 3 does not include any hydrogen bonds with a distance exceeding 5 Å.

3.3. Robustness of the Docked Conformations. The RMSD range for MAPK3 backbone atoms bound to emodin-8-glucoside was computed between 1.6 and 2.28 Å following 100 ns computer simulation. The RMSD value for a free receptor, however, was found to be between 1.55 and 2.57 Å. In the case of the enzyme complexed with ulixertinib, the minimum and maximum RMSD values were found to be 1.25 and 2.02 Å, respectively. The receptor exhibited more excellent stability when in complex with emodin-8-glucoside in comparison to being free, as suggested by the results. The simulation results showed that the protein's backbone atoms remained stable after approximately 70 ns of simulation when hindered by emodin-8-glucoside, as indicated in Figure 3(a).

As per the RMSF plots, a notable difference in fluctuation was observed around the 64–124 region. Specifically, the fluctuation of protein complexed with emodin-8-glucoside was lower than that of the free protein (Figure 3(b)). Given the proximity of this region to the MAPK3 active site [19], emodin-8-glucoside is believed to have stabilized the protein's active site. However, the MAPK3 active site appears to have been more stabilized by the reference drug than by emodin-8-glucoside.

The MAPK3-emodin-8-glucoside total energy was found to be lower than that of free protein during the 100 ns MD simulations. As well, the total energy exhibited by MAPK3-ulixertinib was the lowest compared to that of free MAPK3 and MAPK3-emodin-8-glucoside during the 100 ns MD simulation, according to Figure 3(c).

The results revealed that the ROG value of free MAPK3, MAPK3-ulixertinib, and MAPK3-emodin-8-glucoside increased after the 100 ns MD simulation. As per the data presented in Figure 3(d), the ROG for the enzyme complexed with emodin-8-glucoside was lower than that of free MAPK3 during the first 50 ns computer simulation. Throughout the 50–100 ns MD simulation range, the ROG values of free MAPK3, MAPK3-ulixertinib, and MAPK3-

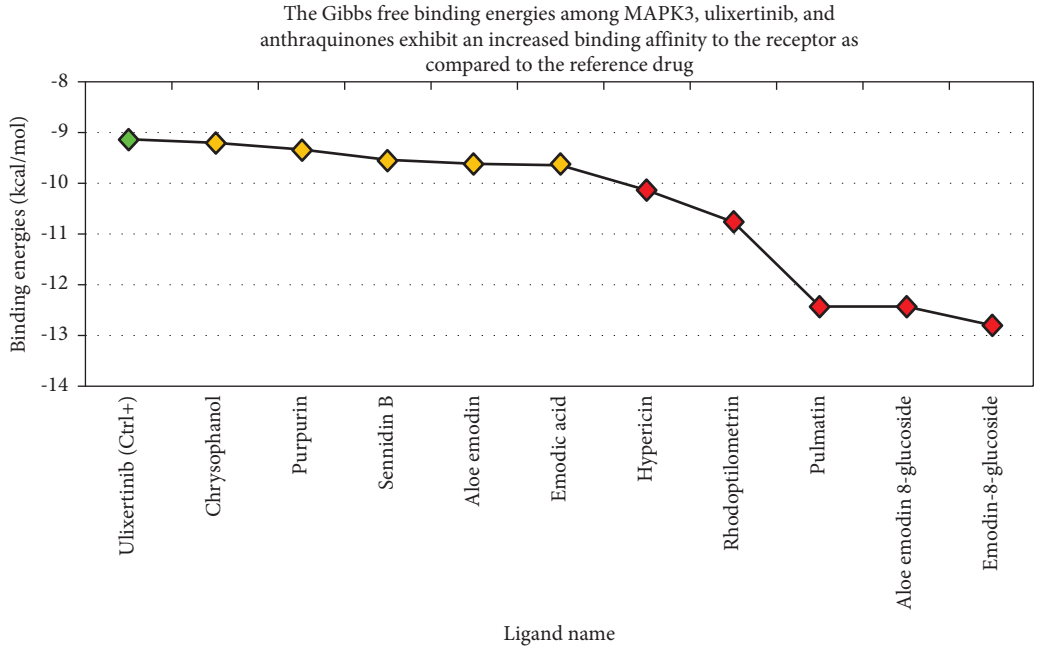

FIGURE 1: The $\Delta G_{binding}$ values indicate the Gibbs free binding energy in kcal/mol units between anthraquinones, the MAPK3 positive control inhibitor, and the receptor's active site. Ligand names are shown on the *X*-axis, and their corresponding Gibbs free binding energy is presented on the *Y*-axis. The green diamond represents the positive control inhibitor, the red spots depict the most potent MAPK3 inhibitors in this study, and the orange spots show compounds with higher binding affinity to MAPK3 than the reference drug. MAPK3, mitogen-activated protein kinase-3.

TABLE 1: The active site of MAPK3 was evaluated for Gibbs free energy and *K*i values in the presence of 21 anthraquinones, along with a positive control inhibitor.

PubChem ID	Ligand name	$\Delta G_{binding}$	Inhibition constant
(A) Anthraquinones			
99649	Emodin-8-glucoside	−12.78	430.14 pM
126456371	Aloe emodin 8-glucoside	−12.42	790.15 pM
442731	Pulmatin (chrysophanol-8-0-glucoside)	−12.41	793.77 pM
101286218	Rhodoptilometrin	−10.75	13.14 nM
3663	Hypericin	−10.13	37.48 nM
361510	Emodic acid	−9.64	86.15 nM
10207	Aloe-emodin	−9.63	86.80 nM
10459879	Sennidin B	−9.52	105.35 nM
6683	Purpurin	−9.33	145.27 nM
10208	Chrysophanol	−9.19	184.75 nM
10168	Rhein	−9.09	216.30 nM
3220	Emodin	−8.85	327.05 nM
6293	Alizarin	−8.40	500.01 nM
2950	Danthron	−8.38	719.56 nM
92826	Sennidin A	−8.30	828.06 nM
10639	Physcion	−8.18	1.01 μM
160712	Nordamnacanthal	−7.95	1.48 μM
3083575	Obtusifolin	−7.63	2.55 μM
124062	Rubiadin	−7.33	4.24 μM
442753	Knipholone	−6.97	7.72 μM
2948	Damnacanthal	−5.47	98.18 μM
(B) Control inhibitor			
11719003	Ulixertinib	−9.12	207.14 nM

MAPK3, mitogen-activated protein kinase-3.

Table 2: Different energy types are present among the MAPK3 active site, top-ranked anthraquinones, and a positive control inhibitor.

Ligand name	Intermolecular energy (kcal/mol)	Total internal energy (kcal/mol)	Torsional free energy (kcal/mol)	Unbound system's energy (kcal/mol)	Free binding energy (kcal/mol)
(A) Anthraquinones					
Emodin-8-glucoside	−11.32	−6.21	+3.28	−1.48	−12.78
Aloe emodin 8-glucoside	−11.25	−6.14	+3.58	−1.39	−12.42
Pulmatin (chrysophanol-8-0-glucoside)	−10.48	−6.41	+2.98	−1.49	−12.41
Rhodoptilometrin	−11.44	−2.18	+2.39	−0.49	−10.75
Hypericin	−8.08	−4.69	+2.39	−0.26	−10.13
(B) Control inhibitor					
Ulixertinib	−8.36	−3.57	+2.39	−0.42	−9.12

MAPK3, mitogen-activated protein kinase-3.

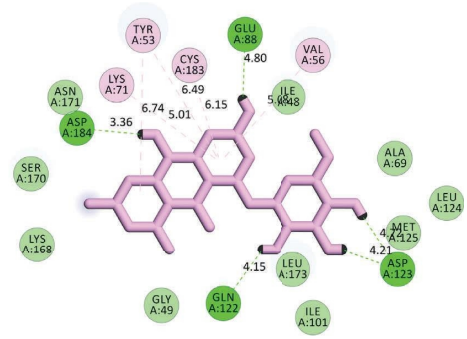

Interactions
- van der Waals
- Conventional Hydrogen Bond
- Alkyl
- Pi-Alkyl

(a)

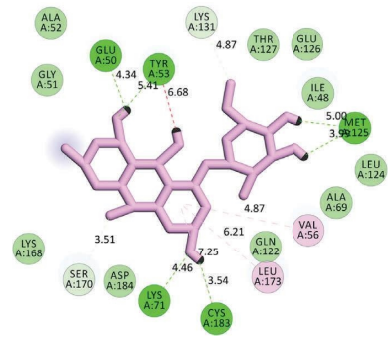

Interactions
- van der Waals
- Conventional Hydrogen Bond
- Carbon Hydrogen Bond
- Unfavorable Donor-Donor
- Alkyl

(b)

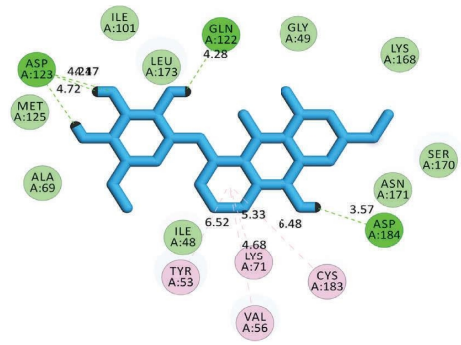

Interactions
- van der Waals
- Conventional Hydrogen Bond
- Alkyl
- Pi-Alkyl

(c)

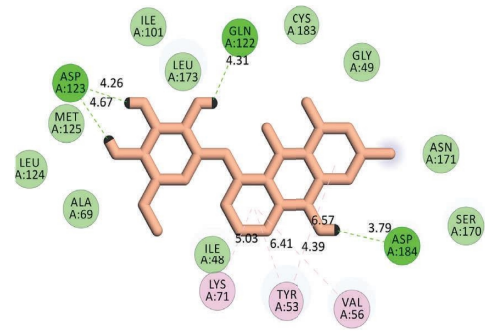

Interactions
- van der Waals
- Conventional Hydrogen Bond
- Alkyl
- Pi-Alkyl

(d)

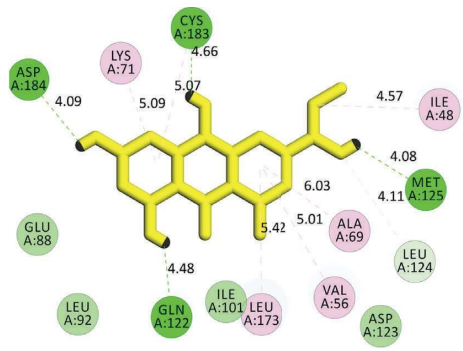

Interactions
- van der Waals
- Conventional Hydrogen Bond
- Carbon Hydrogen Bond
- Alkyl

(e)

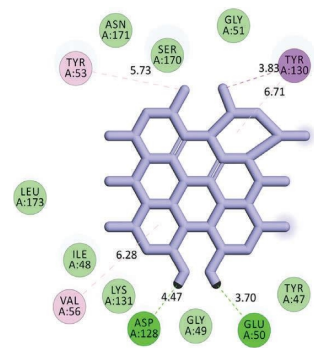

Interactions
- van der Waals
- Conventional Hydrogen Bond
- Pi-Sigma
- Alkyl
- Pi-Alkyl

(f)

Figure 2: Continued.

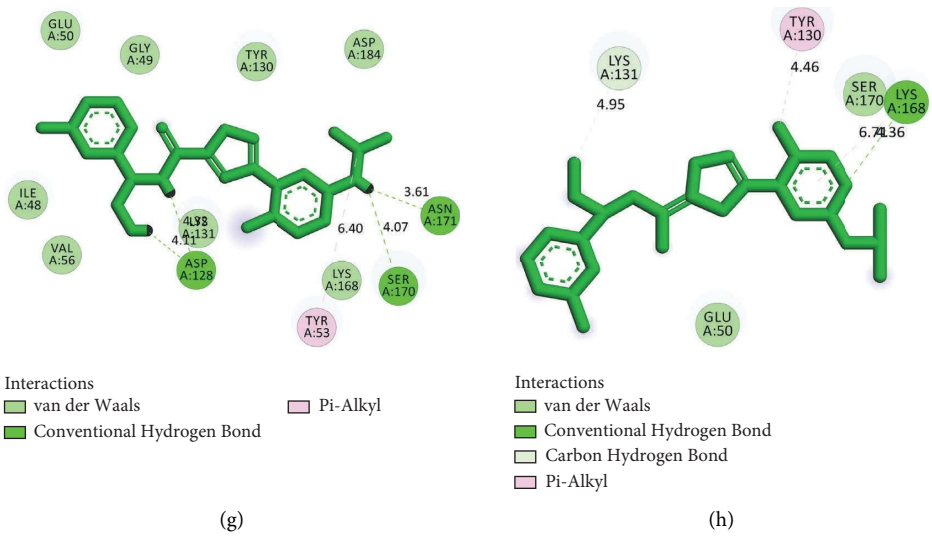

(g) (h)

FIGURE 2: Various interaction modes were observed between the top-ranked anthraquinones, the reference drug, and residues inside the MAPK3 active site. Emodin-8-glucoside is displayed in (a, b), and the reference drug is shown before and after MD simulations in (g, h), respectively. Other anthraquinones, such as aloe emodin 8-glucoside, pulmatin, rhodoptilometrin, and hypericin, are illustrated in (c), (d), (e), and (f), respectively. MD, molecular dynamics; MAPK3, mitogen-activated protein kinase-3.

emodin-8-glucoside were in close proximity to each other. The superimposed structures of free MAPK3, MAPK3-emodin-8-glucoside, and MAPK3-ulixertinib, before and after MD simulations, are presented in Figure 4, using the DSV tool. In addition, Figure 5 depicts the incorporation of emodin-8-glucoside in the MAPK3 ATP-binding grove, both pre- and post-MD simulation, carried out with the help of Chimera version 1.8.1.

4. Discussion

The MAPK3 gene encodes an upstream regulator of the MAPK cascade that plays a crucial role in various biological processes associated with apoptosis and cell survival. Aberrant expression of MAPK3 has been linked to the initiation, progression, metastasis, and resistance to the treatment of various human cancers, highlighting the urgent need to explore and develop innovative and potent MAPK3 inhibitors [19]. The objective of this study was to identify natural AQs that could serve as promising inhibitors of MAPK3. The results indicated that the calculated binding free energy between MAPK3 and five AQs (emodin-8-glucoside, aloe emodin 8-glucoside, pulmatin, rhodoptilometrin, and hypericin) was <−10 kcal/mol, making them the most potent MAPK3 inhibitors in this study. The recorded $\Delta G_{binding}$ value of −9.12 kcal/mol between MAPK3 and ulixertinib indicates that the top-ranked AQs in this study had a stronger binding affinity to the MAPK3 ATP-binding cleft compared to the standard drug. Furthermore, emodin-8-glucoside, aloe emodin 8-glucoside, and pulmatin exhibited *K*i values in the picomolar range.

The MAPK3 active site exhibited a $\Delta G_{binding}$ value of −12.78 kcal/mol upon binding with emodin-8-glucoside. Furthermore, the binding energies between aloe emodin 8-glucoside, aloe-emodin, emodin, and MAPK3 were estimated to be −12.42, −9.63, and −8.85 kcal/mol, respectively. These results suggest a sugar moiety enhances emodin's binding affinity to MAPK3. Prior to undergoing MD simulations, emodin-8-glucoside was shown to establish five hydrogen and five hydrophobic interactions with residues Tyr53, Val56, Lys71, Glu88, Gln122, Asp123, Cys183, and Asp184 situated within the ATP-binding cleft of MAPK3. This compound exhibited seven H-bonds and three hydrophobic interactions with Glu50, Val56, Lys71, Met125, Lys131, Ser170, Leu173, and Cys183, after MD simulations.

The use of Chinese herbs to treat different cancers has been established for a long time due to their confirmed benefits and negligible side effects. Emodin (1,3,8-trihydroxy-6-methylanthraquinone) is obtained from the root and rhizome of *Rheum palmatum* L., a medicinal herb with a long-standing tradition [43]. Previous research has demonstrated that emodin possesses inhibitory potential against several cancers, such as hepatocellular carcinoma [44], breast cancer [45], cervical cancer [46], ovarian cancer [47], and bladder cancer [48]. According to Manimaran et al. [49], emodin administration at a dose of 50 mg/kg b.w. was effective in inhibiting the activation of Akt, ERK, P38 MAPK, and DNA methyl transferase (DNMT) in golden Syrian hamsters with 7,12-dimethylbenz[a]anthracene (DMBA)-induced oral carcinoma. This was evident from the downregulation of these markers as observed through Western blotting. Furthermore, emodin was found to alleviate the severity of precancerous lesions, such as dysplasia, in DMBA-treated hamsters. As well, the findings of Lin et al. [50] indicate that aloe emodin can suppress the expression of matrix metalloproteinase-2 via the P38 MAPK-NF-kappa B signaling pathway, thereby inhibiting the invasion of nasopharyngeal carcinoma cells.

According to the findings, the binding of chrysophanol-8-0-glucoside (pulmatin) to the MAPK3 catalytic domain

Table 3: Multiple modes of interactions between the catalytic site of MAPK3, top-ranked anthraquinones, and a positive control inhibitor.

Ligand name	Hydrogen bond (distance A)	Hydrophobic interaction (distance A)
(A) Anthraquinones		
Emodin-8-glucoside (before MD)	Asp184 (3.36); Glu88 (4.80); Asp123 (4.72, 4.21); Gln122 (4.15)	Tyr53 (6.74, 6.49); Cys183 (6.15); Val56 (5.08); Lys71 (5.01)
Emodin-8-glucoside (after MD)	Glu50 (4.34); Lys131 (4.87); Met125 (3.99, 5.0); Lys71 (4.46); Cys183 (3.54); Ser170 (3.51)	Val56 (4.87); Leu173 (6.21); Cys183 (7.25)
Aloe emodin 8-glucoside	Asp123 (4.72, 4.21, 4.47); Gln122 (4.28); Asp184 (3.57)	Tyr53 (6.52); Cys183 (6.48); Val56 (4.68); Lys71 (5.33)
Pulmatin (chrysophanol-8-0-glucoside)	Asp123 (4.67, 4.26); Gln122 (4.31); Asp184 (3.79)	Tyr53 (6.57, 6.41); Val56 (4.39); Lys71 (5.03)
Rhodoptilometrin	Asp184 (4.09); Cys183 (4.66); Met125 (4.08); Leu124 (4.11); Gln122 (4.48)	Lys71 (5.09); Cys183 (5.07); Ile48 (4.57); Ala69 (6.03); Val56 (5.01); Leu173 (5.42)
Hypericin	Asp128 (4.47); Glu50 (3.70)	Tyr130 (6.71, 3.83); Tyr53 (5.73); Val56 (6.28)
Ulixertinib (before MD)	Asn171 (3.61); ser170 (4.07); Asp128 (4.11, 4.32)	Tyr53 (6.4)
Ulixertinib (after MD)	Lys168 (4.36); Lys131 (4.95)	Tyr130 (4.46); Lys168 (6.71)

MAPK3, mitogen-activated protein kinase-3.

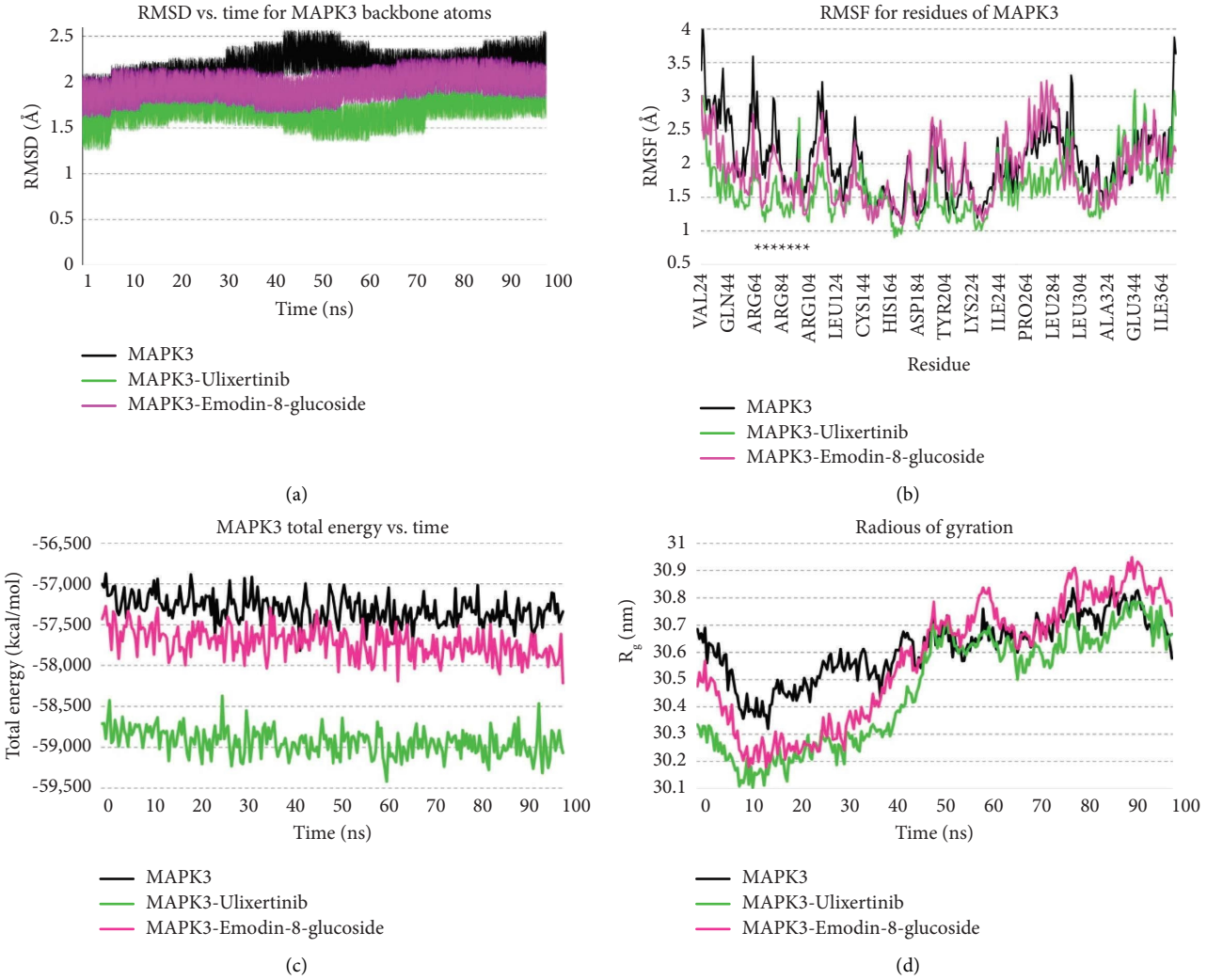

Figure 3: Through the generation of (a) RMSD, (b) RMSF, (c) total energy, and (d) radius of gyration plots, the behavior of free MAPK3 backbone atoms was analyzed in the presence of emodin-8-glucoside and ulixertinib during a 100 ns MD simulation. The location of the asterisks in part (b) is within the protein's active site. MAPK3, mitogen-activated protein kinase-3; RMSF, root mean square fluctuation; RMSD, root-mean-square deviations; MD, molecular dynamics.

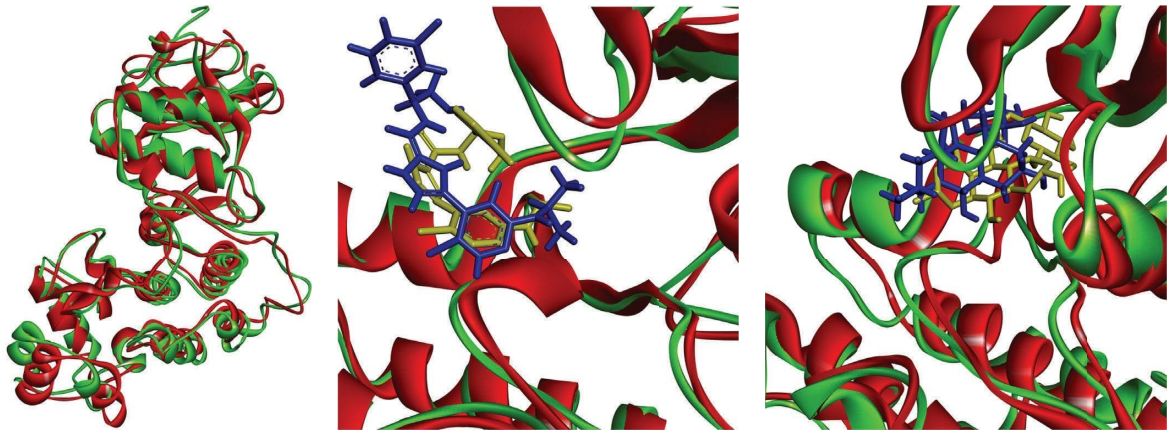

Figure 4: The structures of (a) free MAPK3, (b) MAPK3 in the presence of ulixertinib, and (c) MAPK3 in the presence of emodin-8-glucoside were superimposed after a 100 ns MD simulation. The protein chains before and after the MD analysis are depicted in green and red, respectively, while the ligands before and after the MD simulations are displayed in yellow and blue colors. MAPK3, mitogen-activated protein kinase-3; MD, molecular dynamics.

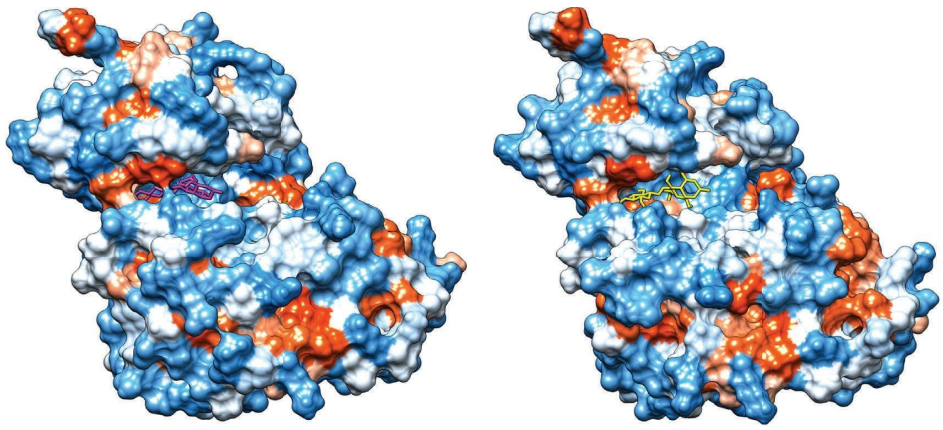

(a) (b)

Figure 5: The hydrophobicity surface mode of MAPK3 in a 3D view is depicted. Emodin-8-glucoside is depicted within the MAPK3 ATP-binding grove in (a, b), before and after a 100 ns MD simulation, respectively. MAPK3, mitogen-activated protein kinase-3; MD, molecular dynamics.

resulted in a *K*i value of 793.77 pM and a binding energy of −12.41 kcal/mol. The MAPK3 showed less binding affinity towards chrysophanol than its glycosylated form, with a recorded $\Delta G_{binding}$ value of −9.19 kcal/mol and a *K*i value of 184.75 nM. The MAPK3 active site was found to interact with chrysophanol-8-0-glucoside through four hydrogen and four hydrophobic interactions with specific residues, including Tyr53, Val56, Lys71, Gln122, Asp123, and Asp184, before MD simulations.

Chrysophanol, an anthraquinone metabolite obtained from the *Rheum genus*, has been found to possess anticancer properties in recent studies [51–53]. In addition, it exhibits anti-inflammatory activity [54] and provides neuroprotection effects [55]. *Rheum genus* contains a higher amount of chrysophanol-8-O-glucoside, which is a glycosylated form of chrysophanol, compared to chrysophanol [56]. Our bioinformatics results are in line with those of the research of Kwon et al. [57], who have found that the *Cassia tora* seed extract, a rich source of chrysophanol, can deactivate the JNK/P38 MAPK signaling pathway, thereby suppressing heat-induced lipogenesis in human sebocytes.

Upon conducting a comparison of the "emodin-8-glucoside"-MAPK3 contacts between the initial docking and final MD-simulated results, several noteworthy points emerged. These are as follows:

(a) The hydrophobic interaction between Val56, Cys183, and emodin-8-glucoside remained stable before and after the MD simulation.

(b) Cys183 formed a hydrogen bond with emodin-8-glucoside in addition to the hydrophobic interaction after the MD simulation.

(c) The contact between emodin-8-glucoside and Lys71 was initially a hydrophobic interaction, while after the MD simulation, it was observed as a hydrogen bond.

(d) Following the MD simulation, new residues interacted with the emodin-8-glucoside, including Glu50, Met125, Lys131, Ser170, and Leu173.

Furthermore, the results indicated that the interacting residues between MAPK3 and ulixertinib underwent a complete change following the MD simulation. Prior to the simulation, Tyr53, Asp128, Ser170, and Asn171 were found to interact with ulixertinib. However, after the simulation, hydrophobic and hydrogenic interactions were observed between Tyr130, Lys131, and Lys168 and the reference drug. It is worth noting that, based on the present findings, the interactions between emodin-8-glucoside and MAPK3 were comparatively more stable than those observed with the standard drug.

5. Conclusion

Based on the current study, emodin-8-glucoside, aloe-emodin 8-glucoside, pulmatin, rhodoptilometrin, and hypericin possess strong inhibitory properties against MAPK3. Among these metabolites, emodin-8-glucoside, aloe-emodin 8-glucoside, and pulmatin are the most potent, with *K*i values at the picomolar scale. The computer simulation indicated that the 3D conformation of MAPK3 remained stable when in complex with emodin-8-glucoside for approximately 65 ns. These findings may offer valuable insights to researchers aiming to create novel drug therapies for numerous types of cancer. However, additional research is needed to confirm the present results, including more extended MD simulations and in vitro and in vivo validation experiments.

Data Availability

The datasets used and/or analyzed during the current study are available from the corresponding author upon reasonable request.

Ethical Approval

The present study was approved by the Ethics Committee of the Hamadan University of Medical Sciences, Hamadan, Iran (ethics no. IR.UMSHA.REC.1401.254).

Conflicts of Interest

The authors declare that they have no conflicts of interest.

Authors' Contributions

AT and SV-A designed the study. MM conducted docking operations. AT performed MD simulations. AT and SV-A analyzed and discussed the results. AT wrote the manuscript. SV-A edited the manuscript. All the authors read and approved the final version of the manuscript.

Acknowledgments

The authors thank the Research Center for Molecular Medicine, Dental Research Center, Hamadan University of Medical Sciences, Hamadan, Iran, for their support.

References

[1] R. Prochazka and L. Nemcova, "Mechanisms of FSH-and amphiregulin-induced MAP Kinase 3/1 activation in pig cumulus-oocyte complexes during maturation in vitro," *International Journal of Molecular Sciences*, vol. 20, no. 5, p. 1179, 2019.

[2] J. Yuan, X. Dong, J. Yap, and J. Hu, "The MAPK and AMPK signalings: interplay and implication in targeted cancer therapy," *Journal of Hematology & Oncology*, vol. 13, no. 1, p. 113, 2020.

[3] L. Santarpia, S. M. Lippman, and A. K. El-Naggar, "Targeting the MAPK-RAS-RAF signaling pathway in cancer therapy," *Expert Opinion on Therapeutic Targets*, vol. 16, no. 1, pp. 103–119, 2012.

[4] C. Braicu, M. Buse, C. Busuioc et al., "A comprehensive review on MAPK: a promising therapeutic target in cancer," *Cancers*, vol. 11, no. 10, p. 1618, 2019.

[5] A. S. Dhillon, S. Hagan, O. Rath, and W. Kolch, "MAP kinase signalling pathways in cancer," *Oncogene*, vol. 26, no. 22, pp. 3279–3290, 2007.

[6] A. B. Turke, Y. Song, C. Costa et al., "MEK inhibition leads to PI3K/AKT activation by relieving a negative feedback on ERBB receptors," *Cancer Research*, vol. 72, no. 13, pp. 3228–3237, 2012.

[7] M. C. Mendoza, E. E. Er, and J. Blenis, "The Ras-ERK and PI3K-mTOR pathways: cross-talk and compensation," *Trends in Biochemical Sciences*, vol. 36, no. 6, pp. 320–328, 2011.

[8] T. Rampias, A. Giagini, S. Siolos et al., "RAS/PI3K crosstalk and cetuximab resistance in head and neck squamous cell carcinoma," *Clinical Cancer Research*, vol. 20, no. 11, pp. 2933–2946, 2014.

[9] I. Gkouveris, N. Nikitakis, M. Karanikou, G. Rassidakis, and A. SklavOUNOU, "Erk1/2 activation and modulation of STAT3 signaling in oral cancer," *Oncology Reports*, vol. 32, no. 5, pp. 2175–2182, 2014.

[10] H.-L. Ngan, Y. Liu, A. Y. Fong et al., "MAPK pathway mutations in head and neck cancer affect immune microenvironments and ErbB3 signaling," *Life Science Alliance*, vol. 3, no. 6, Article ID e201900545, 2020.

[11] H. L. Ngan, C. H. Law, Y. C. Y. Choi, J. Y. Chan, and V. W. Y. Lui, "Precision drugging of the MAPK pathway in head and neck cancer," *NPJ genomic medicine*, vol. 7, no. 1, p. 20, 2022.

[12] Z. Bayat, Z. Farhadi, and A. Taherkhani, "Identification of potential biomarkers associated with poor prognosis in oral squamous cell carcinoma through integrated bioinformatics analysis: a pilot study," *Gene Reports*, vol. 24, Article ID 101243, 2021.

[13] Y. Zhao, H. Liu, A. I. Riker, O. Fodstad, S. P. Ledoux, and G. L. Wilson, "Emerging metabolic targets in cancer therapy," *Frontiers in Bioscience*, vol. 16, no. 1, p. 1844, 2011.

[14] A. Taherkhani, P. Khodadadi, L. Samie, Z. Azadian, and Z. Bayat, "Flavonoids as strong inhibitors of MAPK3: a computational drug Discovery approach," *International Journal of Analytical Chemistry*, vol. 2023, Article ID 8899240, 16 pages, 2023.

[15] H. Cao, C. Xiao, H. Lu et al., "MiR-129 reduces CDDP resistance in gastric cancer cells by inhibiting MAPK3," *European Review for Medical and Pharmacological Sciences*, vol. 23, no. 15, pp. 6478–6485, 2019.

[16] Y. Du, J. Zhang, Y. Meng, M. Huang, W. Yan, and Z. Wu, "MicroRNA-143 targets MAPK3 to regulate the proliferation and bone metastasis of human breast cancer cells," *AMB Express*, vol. 10, no. 1, pp. 134–138, 2020.

[17] T. T. Yu, C. Y. Wang, and R. Tong, "ERBB2 gene expression silencing involved in ovarian cancer cell migration and invasion through mediating MAPK1/MAPK3 signaling pathway," *European Review for Medical and Pharmacological Sciences*, vol. 24, no. 10, pp. 5267–5280, 2020.

[18] Y. Baba, K. Nosho, K. Shima et al., "Prognostic significance of AMP-activated protein kinase expression and modifying effect of MAPK3/1 in colorectal cancer," *British Journal of Cancer*, vol. 103, no. 7, pp. 1025–1033, 2010.

[19] Bayat Zeynab, Tarokhian Aida, and Taherkhani Amir, "Cinnamic acids as promising bioactive compounds for cancer therapy by targeting MAPK3: a computational simulation study," *Journal of Complementary and Integrative Medicine*, 2023.

[20] Y. Li, F. Guo, Y. Guan et al., "Novel anthraquinone compounds inhibit colon cancer cell proliferation via the reactive oxygen species/JNK pathway," *Molecules*, vol. 25, no. 7, p. 1672, 2020.

[21] C. Opoku-Temeng, N. Dayal, M. Aflaki Sooreshjani, and H. O. Sintim, "3H-pyrazolo [4, 3-f] quinoline haspin kinase inhibitors and anticancer properties," *Bioorganic Chemistry*, vol. 78, pp. 418–426, 2018.

[22] E. M. Malik and C. E. Müller, "Anthraquinones as pharmacological tools and drugs," *Medicinal Research Reviews*, vol. 36, no. 4, pp. 705–748, 2016.

[23] K. Xu, P. Wang, L. Wang et al., "Quinone derivatives from the genus Rubia and their bioactivities," *Chemistry and Biodiversity*, vol. 11, no. 3, pp. 341–363, 2014.

[24] K. Chen, B. Z. Chu, F. Liu et al., "New benzimidazole acridine derivative induces human colon cancer cell apoptosis in vitro via the ROS-JNK signaling pathway," *Acta Pharmacologica Sinica*, vol. 36, no. 9, pp. 1074–1084, 2015.

[25] F. Duan, Y. Yu, R. Guan, Z. Xu, H. Liang, and L. Hong, "Vitamin K2 induces mitochondria-related apoptosis in human bladder cancer cells via ROS and JNK/p38 MAPK signal pathways," *PLoS One*, vol. 11, no. 8, Article ID e0161886, 2016.

[26] R. B. Weiss, "The anthracyclines: will we ever find a better doxorubicin?" *Seminars in Oncology*, vol. 19, no. 6, pp. 670–686, 1992.

[27] L. Huang, T. Zhang, S. Li et al., "Anthraquinone G503 induces apoptosis in gastric cancer cells through the mitochondrial pathway," *PLoS One*, vol. 9, no. 9, Article ID e108286, 2014.

[28] A. Koceva-Chyła, M. Jedrzejczak, J. Skierski, K. Kania, and Z. Jóźwiak, "Mechanisms of induction of apoptosis by anthraquinone anticancer drugs aclarubicin and mitoxantrone in comparison with doxorubicin: relation to drug cytotoxicity and caspase-3 activation," *Apoptosis*, vol. 10, no. 6, pp. 1497–1514, 2005.

[29] J. Kluza, P. Marchetti, M. A. Gallego et al., "Mitochondrial proliferation during apoptosis induced by anticancer agents: effects of doxorubicin and mitoxantrone on cancer and cardiac cells," *Oncogene*, vol. 23, no. 42, pp. 7018–7030, 2004.

[30] N. B. Alitheen, A. A. Manaf, S. Yeap, M. Shuhaimi, L. Nordin, and A. Mashitoh, "Immunomodulatory effects of damnacanthal isolated from roots of Morinda elliptica," *Pharmaceutical Biology*, vol. 48, no. 4, pp. 446–452, 2010.

[31] S. K. Burley, C. Bhikadiya, C. Bi et al., "RCSB Protein Data Bank: powerful new tools for exploring 3D structures of biological macromolecules for basic and applied research and education in fundamental biology, biomedicine, biotechnology, bioengineering and energy sciences," *Nucleic Acids Research*, vol. 49, no. D1, pp. D437–D451, 2021.

[32] C. C. Chen and O. Herzberg, "Inhibition of β-lactamase by clavulanate: trapped intermediates in cryocrystallographic studies," *Journal of Molecular Biology*, vol. 224, no. 4, pp. 1103–1113, 1992.

[33] A. Chaikuad, E. M C Tacconi, J. Zimmer et al., "A unique inhibitor binding site in ERK1/2 is associated with slow binding kinetics," *Nature Chemical Biology*, vol. 10, no. 10, pp. 853–860, 2014.

[34] D. S. Wishart, Y. D. Feunang, A. C. Guo et al., "DrugBank 5.0: a major update to the DrugBank database for 2018," *Nucleic Acids Research*, vol. 46, no. D1, pp. D1074–D1082, 2018.

[35] A. Taherkhani, S. Moradkhani, A. Orangi, and A. Jalalvand, "In silico study of some natural anthraquinones on matrix metalloproteinase inhibition," *Research Journal of Pharmacognosy*, vol. 8, no. 4, pp. 37–51, 2021.

[36] Y. Dinakarkumar, J. R. Rajabathar, S. Arokiyaraj et al., "Anti-methanogenic effect of phytochemicals on methyl-coenzyme M reductase—potential: in silico and molecular docking studies for environmental protection," *Micromachines*, vol. 12, no. 11, p. 1425, 2021.

[37] A. Taherkhani, A. Orangi, S. Moradkhani, and Z. Khamverdi, "Molecular docking analysis of flavonoid compounds with matrix metalloproteinase-8 for the identification of potential effective inhibitors," *Letters in Drug Design and Discovery*, vol. 18, no. 1, pp. 16–45, 2021.

[38] O. Trott and A. J. Olson, "AutoDock Vina: improving the speed and accuracy of docking with a new scoring function, efficient optimization, and multithreading," *Journal of Computational Chemistry*, vol. 31, no. 2, pp. 455–461, 2010.

[39] M. Masumi, F. Noormohammadi, F. Kianisaba, F. Nouri, M. Taheri, and A. Taherkhani, "Methicillin-Resistant*Staphylococcus aureus*: docking-based virtual screening and molecular dynamics simulations to identify potential penicillin-binding protein 2a inhibitors from natural flavonoids," *International journal of microbiology*, vol. 2022, Article ID 9130700, 14 pages, 2022.

[40] S. Moradkhani, A. Farmani, M. Saidijam, and A. Taherkhani, "COVID-19: docking-based virtual screening and molecular dynamics study to identify potential SARS-CoV-2 spike protein inhibitors from plant-based phenolic compounds," *Acta Virologica*, vol. 65, no. 03, pp. 288–302, 2021.

[41] A. Taherkhani, S. Moradkhani, A. Orangi, A. Jalalvand, and Z. Khamverdi, "Molecular docking study of flavonoid compounds for possible matrix metalloproteinase-13 inhibition," *Journal of Basic and Clinical Physiology and Pharmacology*, vol. 32, no. 6, pp. 1105–1119, 2021.

[42] Z. Khamverdi, Z. Mohamadi, and A. Taherkhani, "Molecular docking and dynamics simulation of natural phenolic compounds with GSK-3β: a putative target to combat mortality in patients with COVID-19," *Recent advances in inflammation & allergy drug discovery*, vol. 15, no. 1, pp. 16–34, 2022.

[43] J. Jiang, N. Zhou, P. Ying, T. Zhang, R. Liang, and X. Jiang, "Emodin promotes apoptosis of human endometrial cancer through regulating the MAPK and PI3K/AKT pathways," *Open Life Sciences*, vol. 13, no. 1, pp. 489–496, 2019.

[44] W. Lin, M. Zhong, H. Yin et al., "Emodin induces hepatocellular carcinoma cell apoptosis through MAPK and PI3K/AKT signaling pathways in vitro and in vivo," *Oncology Reports*, vol. 36, no. 2, pp. 961–967, 2016.

[45] S. Iwanowycz, J. Wang, J. Hodge, Y. Wang, F. Yu, and D. Fan, "Emodin inhibits breast cancer growth by blocking the tumor-promoting feedforward loop between cancer cells and macrophages," *Molecular Cancer Therapeutics*, vol. 15, no. 8, pp. 1931–1942, 2016.

[46] W. Yaoxian, Y. Hui, Z. Yunyan, L. Yanqin, G. Xin, and W. Xiaoke, "Emodin induces apoptosis of human cervical cancer hela cells via intrinsic mitochondrial and extrinsic death receptor pathway," *Cancer Cell International*, vol. 13, no. 1, pp. 71–78, 2013.

[47] J. Ma, J. Yang, C. Wang et al., "Emodin augments cisplatin cytotoxicity in platinum-resistant ovarian cancer cells via ROS-dependent MRP1 downregulation," *BioMed Research International*, vol. 2014, Article ID 107671, 8 pages, 2014.

[48] X. Li, H. Wang, J. Wang et al., "Emodin enhances cisplatin-induced cytotoxicity in human bladder cancer cells through ROS elevation and MRP1 downregulation," *BMC Cancer*, vol. 16, pp. 578–610, 2016.

[49] A. Manimaran, S. Manoharan, and M. Neelakandan, "Emodin efficacy on the akt, MAPK, ERK and DNMT expression pattern during dmba-induced oral carcinoma in golden SYRIAN hamsters," *African Journal of Traditional, Complementary and Alternative Medicines*, vol. 13, no. 6, pp. 186–193, 2016.

[50] M. L. Lin, Y. C. Lu, J. G. Chung et al., "Down-regulation of MMP-2 through the p38 MAPK-NF-κB-dependent pathway by aloe-emodin leads to inhibition of nasopharyngeal carcinoma cell invasion: aloe-emodin inhibits human NPC cell invasion," *Molecular Carcinogenesis*, vol. 49, no. 9, pp. 783–797, 2010.

[51] C. C. Lu, J. S. Yang, A. C. Huang et al., "Chrysophanol induces necrosis through the production of ROS and alteration of ATP levels in J5 human liver cancer cells," *Molecular Nutrition & Food Research*, vol. 54, no. 7, pp. 967–976, 2010.

[52] C. H. Ni, C. S. Yu, H. F. Lu et al., "Chrysophanol-induced cell death (necrosis) in human lung cancer A549 cells is mediated through increasing reactive oxygen species and decreasing the level of mitochondrial membrane potential," *Environmental Toxicology*, vol. 29, no. 7, pp. 740–749, 2014.

[53] T. Wang, Z. Lu, X.-H. Qu et al., "Chrysophanol-8-O-glucoside protects mice against acute liver injury by inhibiting autophagy in hepatic stellate cells and inflammatory response in liver-resident macrophages," *Frontiers in Pharmacology*, vol. 13, Article ID 951521, 2022.

[54] F. He, N.-N. Liang, L. Mu et al., "Anthocyanins and their variation in red wines II. Anthocyanin derived pigments and their color evolution," *Molecules*, vol. 17, no. 2, pp. 1483–1519, 2012.

[55] X. Chu, S. Zhou, R. Sun et al., "Chrysophanol relieves cognition deficits and neuronal loss through inhibition of inflammation in diabetic mice," *Neurochemical Research*, vol. 43, no. 4, pp. 972–983, 2018.

[56] Z. Wang, P. Ma, L. Xu, C. He, Y. Peng, and P. Xiao, "Evaluation of the content variation of anthraquinone glycosides in rhubarb by UPLC-PDA," *Chemistry Central Journal*, vol. 7, pp. 170–211, 2013.

[57] H. C. Kwon, T. Y. Kim, C. M. Lee, K. S. Lee, and K. K. Lee, "Active compound chrysophanol of Cassia tora seeds suppresses heat-induced lipogenesis via inactivation of JNK/p38 MAPK signaling in human sebocytes," *Lipids in Health and Disease*, vol. 18, no. 1, p. 135, 2019.